Biosensors and Bioelectronics 141 (2019) 111396

Contents lists available at ScienceDirect

Biosensors and Bioelectronics

journal homepage: www.elsevier.com/locate/bios

Pedestal subwavelength grating metamaterial waveguide ring resonator for ultra-sensitive label-free biosensing

Ching-Wen Chang[a,b], Xiaochuan Xu[a,c,*], Swapnajit Chakravarty[a,c], Hui-Chun Huang[d], Li-Wei Tu[b,e], Quark Yungsung Chen[b], Hamed Dalir[a,c], Michael A. Krainak[f], Ray T. Chen[a,c,**]

[a] Department of Electrical and Computer Engineering, The University of Texas at Austin, Austin, TX, 78758, USA
[b] Department of Physics and Center of Crystal Research, National Sun Yat-sen University, Kaohsiung, 80424, Taiwan, ROC
[c] Omega Optics Inc, 8500 Shoal Creek Blvd, Austin, TX, 78759, USA
[d] Department of Materials and Optoelectronic Science, National Sun Yat-sen University, Kaohsiung, 80424, Taiwan, ROC
[e] Department of Medical Laboratory Science and Biotechnology, Kaohsiung Medical University, Kaohsiung, 80708, Taiwan, ROC
[f] NASA Goddard Space Flight Center, Greenbelt, MD, 20771, USA

ARTICLE INFO

Keywords:
Pedestal structures
Subwavelength grating metamaterial
Microring resonator
Optical biosensor

ABSTRACT

Mode volume overlap factor is one of the parameters determining the sensitivity of a sensor. In past decades, many approaches have been proposed to increase the mode volume overlap. As the increased mode volume overlap factor results in reduced mode confinement, the maximum value is ultimately determined by the micro- and nano-structure of the refractive index distribution of the sensing devices. Due to the asymmetric index profile along the vertical direction on silicon-on-insulator platform, further increasing the sensitivity of sub-wavelength grating metamaterial (SGM) waveguide based sensors is challenging. In this paper, we propose and demonstrate pedestaled SGM which reduces the asymmetricity and thus allows further increasing the interaction between optical field and analytes. The pedestal structure can be readily formed by a controlled undercut etching. Both theoretical analysis and experimental demonstration show a significant improvement of sensitivity. The bulk sensitivity and surface sensitivity are improved by 28.8% and 1000 times, respectively. The detection of streptavidin at a low concentration of 0.1 ng/mL (~1.67 pM) is also demonstrated through real-time monitoring of the resonance shift. A ~400 fM streptavidin limit of detection is expected with a 0.01nm resolution spectrum analyzer based on the real-time measurement of streptavidin detection results from two-site binding model fitting.

1. Introduction

Stimulated by the encouraging features such as high sensitivity, high selectivity, high specificity, and rapid response, on-chip photonics biosensors have been receiving considerable attention over the past decades. A large variety of photonic structures have been studied, including ring resonators (Xu et al., 2008; DeVos et al., 2007; Yalçin et al., 2006; Chao et al., 2006; Donzella et al., 2015), surface plasmon resonance (Fan et al., 2015; Miyazaki et al., 2017; Jin et al., 2016), slot waveguides (Tu et al., 2012), and photonic crystals (Yan et al., 2016; Huang et al., 2017; Lueckiger et al., 2016). These photonic biosensors rely on the detection of local refractive index variations induced by the presence of biomolecules on the sensing surface with evanescent waves. Quantitative analysis of the biomolecules can be achieved by monitoring the resonance shift induced by the index variation. Y. Fan et al. used silica nanotube array to demonstrate a surface plasmon resonance sensor with a detection of limit 93 pM detection of limit (Fan et al., 2015). However, surface plasmon resonance sensors or planar waveguide based sensors are difficult to minimize the sensor size and develop to lab on chip by photonic integrated circuits technique. The two-dimensional silicon photonic crystal microcavity biosensor are demonstrated a detection of limit 67 fg/mL (1 fM) detection of limit by varied donor defect modes implantation (Chakravarty et al., 2014a, 2016; Zou et al., 2014). In addition, H. Yan et al. proposed single-input single-output photonic crystal biosensor multi-channel array and the corresponding transmission spectra from each channel without overlap to measure a variety of tumor markers at the same time (Yan et al., 2015). However, the sensitivity of photonic crystal microcavity

* Corresponding author. Department of Electrical and Computer Engineering, The University of Texas at Austin, Austin, TX, 78758, USA.
** Corresponding author. Department of Electrical and Computer Engineering, The University of Texas at Austin, Austin, TX, 78758, USA.
E-mail addresses: xiaochuan.xu@omegaoptics.com (X. Xu), chen@ece.utexas.edu (R.T. Chen).

https://doi.org/10.1016/j.bios.2019.111396
Received 25 March 2019; Received in revised form 23 May 2019; Accepted 31 May 2019
Available online 01 June 2019
0956-5663/

biosensor is lower than microring resonators (Gavela et al., 2016). Among these sensors, silicon-on-insulator (SOI) microring resonators demonstrated great potential because of the high sensitivity (Luan et al., 2018; Luchansky and Bailey, 2012; Washburn et al., 2009; McClellan et al., 2012; Ghasemi et al., 2016; Kim et al., 2013; Iqbal et al., 2010)and compact size. Hundreds of rings can be multiplexed on a single chip to provide competitive through-put compared to conventional testing approaches (Washburn et al., 2009). The bulk sensitivity of strip silicon microring resonator was 57 nm/RIU (Hoste et al., 2014). Talebi Fard et al. improved the sensitivity to 100 nm/RIU through decreasing the waveguide thickness to 90 nm and thus increasing the overlap of the electric field with the analyte (Fard et al., 2014). Many innovative waveguide structures were investigated to further improve the sensitivity of ring resonators, such as slot waveguide (Claes et al., 2009; Zhao et al., 2018), nanoporous materials (Rodriguez et al., 2015; Azuelos et al., 2018), and subwavelength grating metamaterial (SGM) (Yan et al., 2016; Huang et al., 2017; Lueckiger et al., 2016). P. Cheben et al. proposed SGM waveguide concept to couple light between an optical fiber and a planar waveguide in 2006 (Cheben et al., 2006) and demonstrated in 2010 (Bock et al., 2010). As a natural extension, SGM was proposed for chemical and biosensing by several groups (Gonzalo Wangüemert-Pérez et al., 2014; Xu, 2013; Xu and Chen, 2017a, 2017b). The theoretical analysis is first provided by Gonzalo Wangüemert-Pérez et al. (Gonzalo Wangüemert-Pérez et al., 2014). The bulk sensitivity of SGM microring resonator has been experimentally demonstrated to be more than 400 nm/RIU (Flueckiger et al., 2016), which is several times higher than strip microring resonator waveguides. Our group demonstrated an SGM microring resonator with a sensitivity of 440.5 nm/RIU (Yan et al., 2016). However, most microring resonator sensors are fabricated on SOI wafer with a silicon dioxide supported structural framework. It causes an asymmetric index distribution along the vertical direction which sets the maximum overlap factor for all waveguide designs. This limitation can be partially tackled by introducing more symmetricity into the structures. For instance, Gaur et al. utilized suspended silicon strip waveguide microring resonator sensor to improve the sensitivity to 310 nm/RIU (Gaur et al., 2018). The improvement is eminent but still worse than SGM, which could be caused by the increased index contrast along the transverse direction. Another alternative is a pedestal structure (Chao et al., 2006; Lin et al., 2013a, 2013b), which decreases the asymmetric refractive index distribution and provides a firmer structure than suspended structures. The comparison table of microring resonator waveguide sensor is in Table S1.

In this paper, we show that SGM microring resonators with pedestal structure can potentially improve the sensitivity beyond the limit of SOI platform. A 28.8 percent of improvement in bulk sensitivity has been observed experimentally. We also demonstrated the detection of streptavidin with a concentration of 0.1 ng/mL (~1.67 pM), which is 1000 times enhancement compared to previous SGM sensor demonstrations and 10^5 times improvement compared to strip microring sensor. Our results suggest that such pedestal SGM microring resonator has excellent potential for specific biomarkers diagnosis on medical examination in the future.

2. Pedestal subwavelength grating metamaterial waveguide

SGM is formed by arranging multiple materials in a periodic lattice with a subwavelength pitch (Bock et al., 2010; Gonzalo Wangüemert-Pérez et al., 2014; Cheben et al., 2010, 2018; Benedikovic et al., 2017; Oser et al., 2018; Wangüemert-Pérez et al., 2019). A typical SGM waveguide on SOI platform is shown in Fig. 1(a). The macroscopic optical properties of SGM can be readily tailored through controlling the geometric topology of the artificial structures. The potential of using SGM for surface sensing is theoretically proved by Wanguemert-Perez et al. (Wangüemert-Pérez et al., 2019). The sensitivity of all sensors is ultimately determined by the photon-matter interaction if the difference of data acquisition and analysis is not considered. The photon-matter interaction can be quantified as the percentage of optical energy in analytes, which is defined as:

$$f = \frac{\int \varepsilon_{clad}(r) \left|\vec{E}(r)\right|^2 d^3r}{\int \varepsilon(r) \left|\vec{E}(r)\right|^2 d^3r} \quad (1)$$

Here, $\varepsilon(r)$ and $\varepsilon_{clad}(r)$ are dielectric constant distributions of the SGM waveguide and cladding within a period Λ, respectively. $\vec{E}(r)$ is the electric field distribution. f can be readily customized through properly designing the shape and duty cycle (DC) of material inclusions. The maximum achievable f is limited by the asymmetricity of the top and bottom claddings.

The red curves in Fig. 1(c) show the band diagram of quasi-TE modes in a typical SGM waveguide on SOI with a DC of 50%. The width and thickness of the waveguide are 520 nm and 220 nm, respectively. The bottom cladding is silicon dioxide ($n_{sio2} = 1.45$). The top cladding is aqueous solution ($n_{as} = 1.35$), as the SGM is immersed in aqueous solution in biosensing. Since an SGM waveguide can be considered as a conventional waveguide made of a uniform material according to effective medium theory (EMT), the effective refractive index of an SGM waveguide $n_{eff,SGM}$ must follow $n_{eff,SGM} > \max\{n_{top}, n_{bottom}\}$ to support guided modes. As shown by the green curve in Fig. 1(c), the modes of the SGM waveguide must stay below the lightline of SiO_2, which subsequently sets the upper limit of the overlap factor f. As shown by the purple region in Fig. 1(d), the overlap factor of SGM waveguides with DC between 20% and 80% is calculated. The maximum f is ~40% for SGM waveguides on SOI, in which the refractive index distribution along the y direction is asymmetric.

Theoretically, this limitation can be overcome by creating symmetric index distribution along the vertical direction. In this hypothetical scenario, the band diagram and the corresponding overlap factor f are indicated by the blue curves in Fig. 1(c). Due to the symmetricity of the refractive index distribution along y direction, the band is always below n_{as} lightline. Effective index is always larger than n_{as}, the overlap factor could reach more than 90%, as shown by the symmetric case in Fig. 1(d), colored in light green. Although the increased overlap factor leads to the reduced mode confinement, large overlap factor is still beneficial for applications having less stringent requirements on integration density and optical field intensity. In reality, fabricating waveguides floating in aqueous solution is challenging. One alternative is using suspended structures (Gaur et al., 2018; Soler Penadés et al., 2014; Penades et al., 2016; Zhang et al., 2018; Penadés et al., 2017). However, the mechanical strength of suspended structures is always a concern. Besides, to create the suspension structure, the index contrast of the waveguide along the x direction decreases, which prevents f from reaching the theoretical limit. In this paper, we investigate another promising alternative, pedestaled SGM waveguide ring resonators, which could be mechanically more robust than suspended structures. The schematic of the proposed pedestal SGM waveguide on SOI platform is shown in Fig. 1(b). Silicon segments sit on top of pedestals defined by undercut etching with buffered oxide etchant (BOE). For isotropic undercut etching, L equals V, which can be controlled by the etching time. The band diagram of the pedestal SGM waveguide is shown by the red curve in Fig. 1(c). Although the undercut is trivial, the change of the band is significant, especially in the region close to the band edge, as shown in the inset of Fig. 1(c). To assure the mechanical stability, the minimum dimension of I-2L is set as 25 nm. Here, L is the undercut length and I is the thickness of the silicon pillars in the z direction, as shown in the insets of Fig. 1(a) and (b). In Fig. 1(d), the overlap factor of the pedestal SGM waveguide is represented in the red region, Theoretically, the maximum overlap factor of the pedestal SGM waveguide can achieve 55%, which is a significant improvement compared to conventional asymmetric structures on SOI.

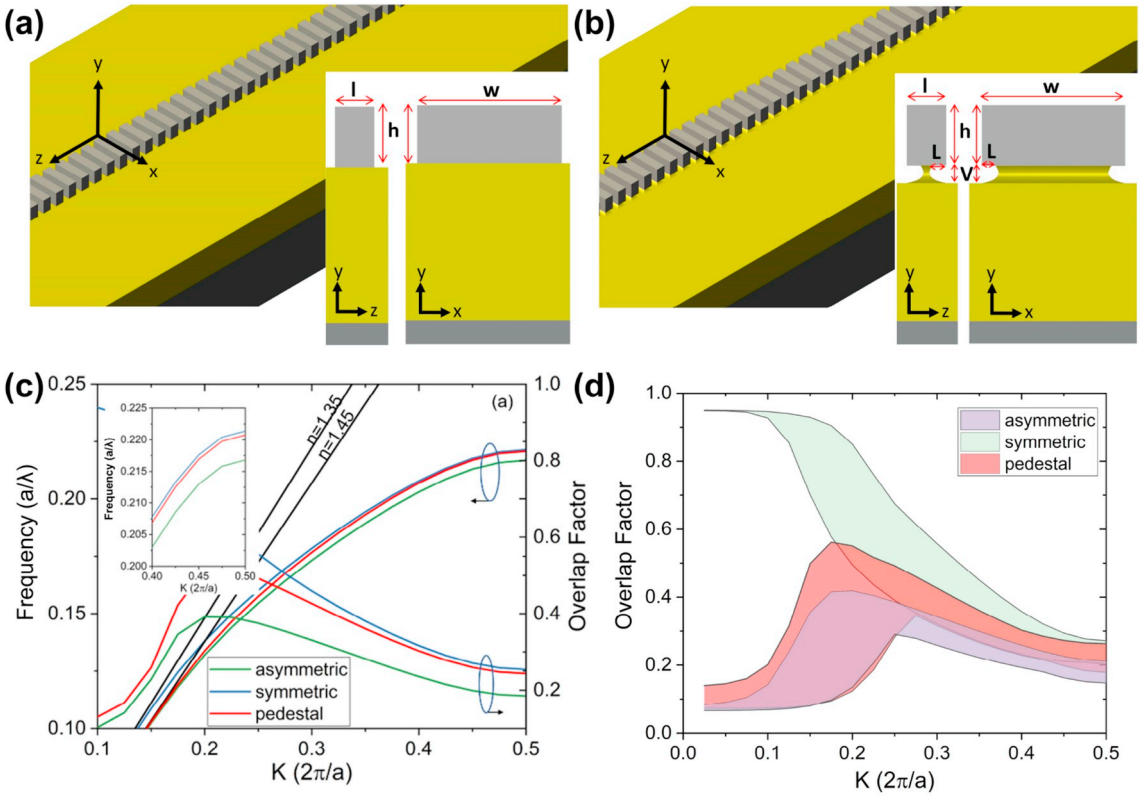

Fig. 1. The schematics of (a) SGM waveguide and (b) pedestal SGM waveguide where gray is silicon and yellow is silicon dioxide. (c) Band diagram of quasi-TE modes and the corresponding overlap factors when the index distribution along the vertical direction is asymmetric (green), symmetric (blue) and pedestal (red). The width of the waveguide is 520 nm, and the thickness is 220 nm. The DC is assumed to be 50%. Inset: magnified view of the band diagram to show the effect of including pedestal. (d) The overlap factors of the three types of SGM waveguides when varying DC from 20% to 80%. With pedestals formed by undercut etching can improve the overlap factor by 20%. (For interpretation of the references to color in this figure legend, the reader is referred to the Web version of this article.)

3. Materials and methods

3.1. SGM ring design and fabrication

According to Hai et al. (Yan et al., 2016), the SGM microring resonators with w = 520 nm, l = 200 nm, and grating period Λ = 250 nm are designed on 220 nm SOI wafer. The gap between the bus waveguide and ring is 50 nm to satisfy the critical coupling condition and thus maximize the quality factor. By utilizing wet etching, pedestal structures are achieved as shown in Fig. 2 (a).

The designed silicon SGM microring resonators were fabricated on SOI chips with 10 nm SiO_2 hard mask layer and 216 nm single crystal Si device layer. The subwavelength pillars were fabricated using electron beam lithography (EBL). Hexamethyldisilazane (HDMS) and diluted ZEP520A photoresist were spin-casted onto a piranha cleaned chip, sequentially. The pattern was first transferred to the resist film by EBL. Then, a two-step dry etching process was used to transfer the pattern to SiO_2 hard mask layer and Si device layer through reactive ion etching. The residual photoresist was then removed by Remover PG. The strip waveguide ring resonator, SGM waveguide ring resonator (Device A) and pedestal SGM ring resonators with different undercut etch time (Device B and Device C) were fabricated. The optical microscope picture of the whole device is shown in Fig. 2 (b). With the "U"-shape configuration, the on-chip circuit can be accessed by a fiber array. The scanning electron microscopy image of the fabricated device are shown in Fig. 2 (c), and the coupling region is shown in Fig. 2 (d). The diameter of all devices is 20 μm. The pedestal structures are fabricated by soaking the chips into BOE to etch buried oxide under the silicon pillars in the microring and bus waveguide. Two etching time, 30 sec and 50 sec, are used for comparison purposes. The xy and yz cross-sections of the silicon pillars are examined by transmission electron microscopy, as shown in Fig. 2 (e)-(h), respectively. Due to the fabrication uncertainty, the fabricated silicon segment is trapezoidal instead of rectangular in xy cross-section, which could decrease the sensitivity. The cross-section views show waveguide width w_{top} = 492 nm, w_{bottom} = 530 nm, the length of rectangular pillar l_{top} = 160 nm and l_{bottom} = 200 nm, and DC = 0.64-0.8. For 30 sec undercut etching time, the lateral etching propagation of short and long sides are 25 nm and 29 nm, while vertical etching propagation of short and long sides are 45 nm and 50 nm. For 50 sec BOE etched device (Device C), the lateral etching propagation of short and long sides are 50 nm, while vertical etching propagation of short and long sides are 65 nm. The structure comparison parameters of all devices are compared in Table S2. In the ideal case, the undercut width should be equal to the etched depth through isotropic wet etching. However, the results show the etching rate of lateral propagation is lower than vertical due to interface adhesion. Before biosensing testing, ~5 nm silicon dioxide layer was grown by thermal wet oxidation at 950 °C for surface chemical treatments and protein immobilization.

3.2. Surface modification

The surface functionalization and probe protein immobilization procedures are depicted in Fig. 3. The self-assembly (3-Aminopropyl) triethoxysilane (APTES) monolayer was formed on the SGM microring surface to provide amine groups (-NH_2) on the silicon dioxide layer for molecular protein binding. Before APTES modification (Fig. 3(a)), hydroxyl groups (-OH) were formed on the SGM microring surface through the piranha treatment for 1 h. Then, the device was rinsed in deionized water and blown dry with nitrogen. After that, the SGM microring sample was silanized by 10% diluted-APTES in pure toluene for 1 h to form silanols (Si-O-H) on the SGM microring surface by the methoxyl group (-CH_3) and the hydroxyl group (-OH) reaction (Fig. 3 (b)). The unbound APTES was removed by thoroughly rinsing the chip

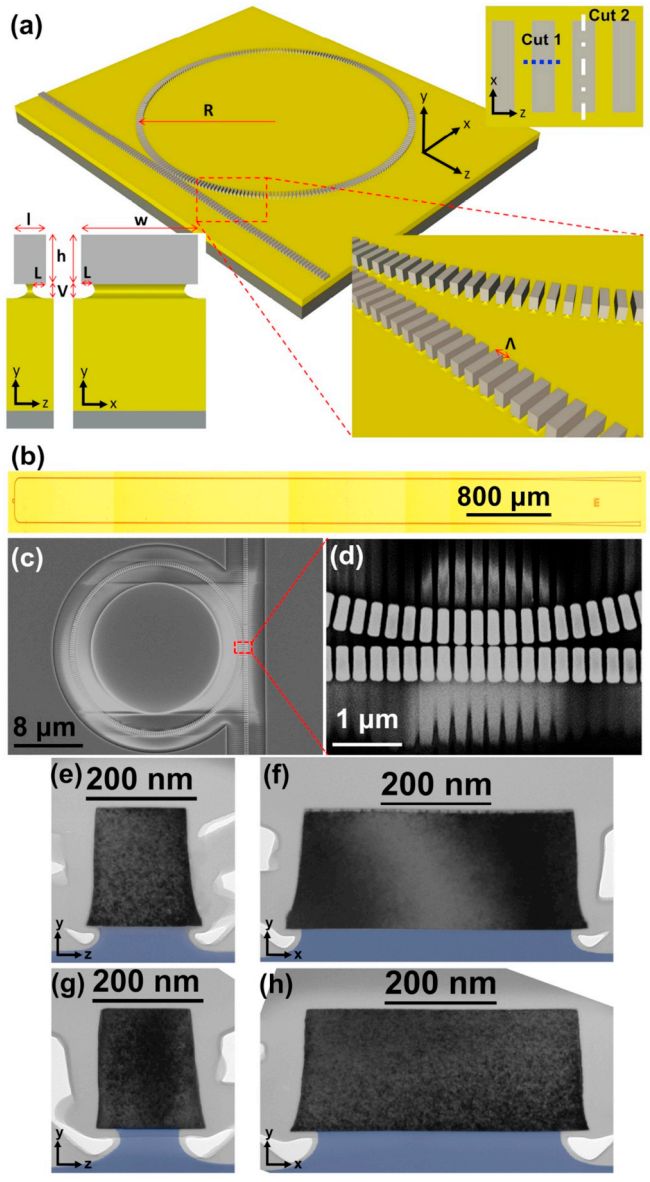

Fig. 2. (a) The schematic of SGM waveguide microring resonator, where R is the diameter of the microring, Λ the subwavelength grating period, h the thickness of waveguide core, *w* the width of waveguide core, l the length of silicon pillar, L the depth of lateral etching propagation, and *V* the depth of vertical etching propagation. (b) The optical microscope image of U-shaped SGM microring biosensor. The SEM images show (c) SGM microring and (d) fine structures of ring and bus waveguide. The 30 sec BOE etched (Device B) buried oxide profile of (e) short side (along with Cut 1) and (f) long side (along with Cut 2) under the silicon pillar. The 50 sec BOE etched (Device C) buried oxide profile of (g) short side (along with Cut 1) and (h) long side (along with Cut 2) under the silicon pillar. (For interpretation of the references to color in this figure legend, the reader is referred to the Web version of this article.)

with toluene and methanol and blowing dry with nitrogen. The chip was baked at 110 °C for 1 h under ambient condition to enhance the stability of the bounded molecules. After APTES modification, 10^{-2} M EZ-Link™ Sulfo-NHS-Biotin (Thermo Scientific™), a receptor of streptavidin resins, was flowed to the APTES/SGM microring through the polydimethylsiloxane (PDMS) channel by syringe pump with a pumping speed of 20 μL/min for 1 h (Fig. 3 (c)). Afterward, the Sulfo-NHS-Biotin immobilized APTES/SGM microring devices were utilized to detect streptavidin resins. The standard streptavidin (SA) powder from streptomyces avidinii (Sigma-Aldrich) was prepared into 0.1 ng/mL, 1 ng/mL, 10 ng/mL, 100 ng/mL, 1 μg/mL, 10 μg/mL and 100 μg/mL in a solution of phosphate-buffered saline (PBS) with 1% bovine serum albumin (BSA) for studying the pedestal SGM microring biosensor surface sensitivity (Fig. 3 (d)). BSA can fill and block the space between APTES molecules to avoid nonspecific bonding. It is notable that 1% BSA added PBS is chosen as the buffer solution because BSA can be supplemented to avoid outflow during each flowing process. Then, the spectra detection can be more stable.

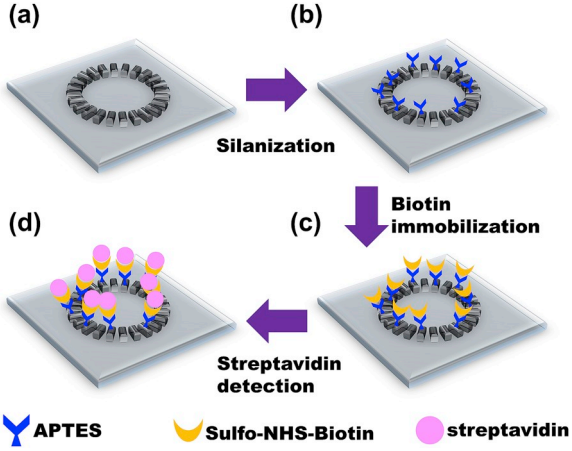

Fig. 3. The procedure of surface modification and detection of SGM microring biosensor: (a) SGM microring with pedestal structure, (b) APTES modification after piranha treatment, (c) Sulfo-NHS-Biotin immobilized, and (d) streptavidin detection.

3.3. Measurement setups

The transmission spectra of SGM microring biosensor were measured by using broadband superluminescent light emitting diodes (SLED) light source covering 1530-1570 nm and C-band optical spectrum analyzer (Optoplex, OM-1C2MM353). The fiber array was utilized for light coupling into and out of the device. The PDMS microfluidic channel was integrated on the test stage and two plastic flow tubes were connected to the PDMS microfluidic channel at both ends. The biomolecules source was injected to microfluidic channel from in-flow tube and a syringe for pumping the bio-molecules was connected to outflow tube for controlling flow rate by a stepping motor. The temperature of the stage was controlled at 25 °C with Newport 3040 temperature controller to avoid thermal effect induced resonance shift during biosensing testing. More details and the schematic of the system are shown in Fig. 3.

4. Results and discussion

4.1. The transmission spectra and bulk sensitivity

The transmission spectra of the SGM microring and pedestal SGM microring are shown in Fig. 4 (a). The free spectral range (FSR) is measured to be ~13 nm, corresponding to a group refractive index $n_g = \frac{\lambda^2}{2\pi R \times FSR} \sim 3$. The estimated quality factor in deionized water is $Q \sim \frac{\lambda_{resonance}}{\Delta\lambda_{3dB}} \sim 1800$ at 1561.41 nm for Device A. To compare bulk refractive index sensitivity of SGM microring and pedestal SGM microring, different concentrations of glycerol solution (0%, 2.5%, 5%, 10%, and 20%) were prepared and injected onto the sensing area through microfluidic channels. The flow rate and time of each diluted glycerol solution are 50 μL/min and 242 sec (for 30 data points), respectively. The resonance peak shifts were monitored and plotted in Fig. 4 (b). The bulk sensitivity of the three devices was calculated by $S = \frac{\Delta\lambda}{\Delta n}$, where S is the bulk sensitivity, $\Delta\lambda$ the resonance shift, and Δn

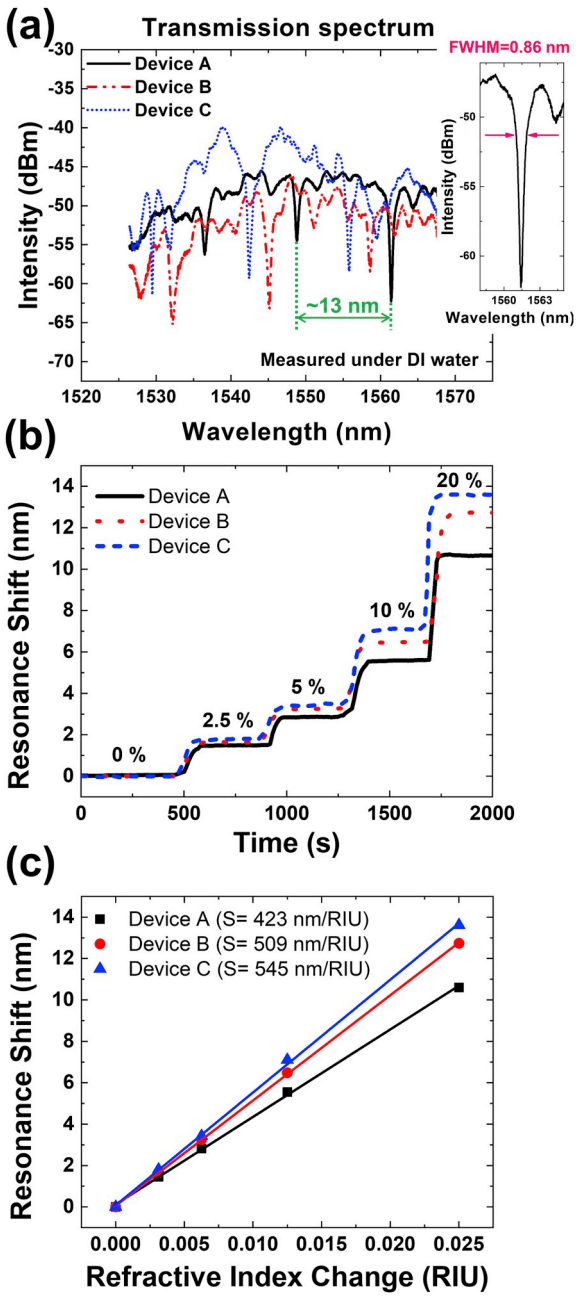

Fig. 4. (a) The transmission spectra of the fabricated SGM microring and pedestal SGM microring. (b) The resonance peak shift was monitored during the bulk refractive index change. (c) The resonance shift versus refractive index change extracted by the linear regression. The bulk sensitivity of three devices were calculated from each slope.

the refractive index change. In accordance with the real-time monitored testing of different glycerol concentrations, the relationship of resonance peak shifts versus refractive index change (RIC) is shown in Fig. 4 (c). The refractive indices of diluted glycerol solution for 0%, 2.5%, 5%, 10%, and 20% are 1.333, 1.337, 1.340, 1.347, and 1.362, respectively (Köser and Wriedt, 1999). A linear function fits well with a regression correlation coefficient $r^2 = 0.999$ for all devices and the bulk sensitivity, S, of three devices were calculated from the slope to be 423 nm/RIU, 509 nm/RIU, and 545 nm/RIU respectively. This result indicates that the bulk sensitivity is enhanced by 28.8% through the pedestal structures by lateral wet etching, which matches the aforementioned theoretical analysis. Additional, the limit of detection (LOD) can be estimated $\sim 3.3 \times 10^{-4}$ RIU with 60 pm noise level by LOD = 3N/S (Chakravarty et al., 2014b), where N is noise and S is sensitivity.

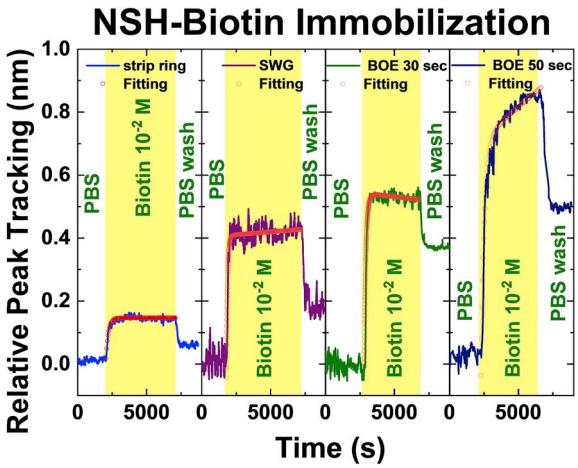

Fig. 5. The real-time relative resonance peak monitored of NHS-biotin immobilization.

4.2. The real-time measurement of NHS-biotin immobilization

After APTES modification, the real-time resonance shift measurement was done to verify that NHS-biotin was immobilized on the sensing area. NHS-biotin is a specific receptor which can bind CA 19-9. For NHS-biotin immobilization, a series of fluids of PBS, 10^{-2} M NHS-biotin diluted in PBS, and again PBS as a wash were introduced sequentially through the PDMS microfluidic channel with a flow rate of 20 μL/min. The first injected PBS was a baseline for subsequent measurement. Fig. 5 shows the significant resonance shifts for all devices.

The dynamic equilibrium of NHS-biotin immobilization was also demonstrated assuming the one-to-one reaction in the microfluidic solution between biotin and APTES which can form a complex biotin-APTES. The kinetic analysis model can be expressed as (Dostálek et al., 2009; Myszka et al., 1998; Fägerstam et al., 1992):

$$[\mathrm{APTES}]_t + [\mathrm{biotin}]_t \leftrightarrow \frac{k_a}{k_d} [\mathrm{APTES} \cdot \mathrm{biotin}]_t, \quad (2)$$

where $[\mathrm{APTES}]_t$ is the concentration of the unbound receptor functionalized on the sample surface, $[\mathrm{biotin}]_t$ the analyte concentration for a solution in the microfluidic channel, and $[\mathrm{APTES} \cdot \mathrm{biotin}]_t$ the concentration of the APTES · biotin complex on the sample surface. The k_a and k_d are effective reaction association and dissociation rate constants. After integration of the pseudo-first-order differential equation, the solution of the kinetics for the association and dissociation is described by the rate law as

$$R(t) = A\left(1 - e^{-(k_a a + k_d)(t - t_a)}\right) \quad (3)$$

where A is the sensor output for equilibrium concentration, as well as t_a and t_d are the start time of association and dissociation phase. Assuming equilibrium concentration for four sensors to be the same due to the identical reaction of the analyte and the receptor, the k_a and k_d are calculated to be $\sim 5 \times 10^3\ M^{-1}s^{-1}$ and $\sim 4 \times 10^{-3}\ s^{-1}$, respectively. It means that $\sim 5 \times 10^3$ APTES · biotin complexes formed per second in a one molar biotin solution and ~0.4% of the complexes decay per second, which indicates that the binding between biotin and APTES is stable. The dissociation constant for the complex is by definition $K_D = k_d/k_a$. Thus, an equilibrium dissociation constant is ~800 nM (Björquist and Boström, 1997), meaning half of the total APTES are occupied with biotin on the sensing area at [biotin] ~ 800 nM (Chang et al., 2018). The wavelength shifts for equilibrium concentration are 0.14 nm, 0.41 nm, 0.54 nm, and 0.71 nm for strip microring resonator, Device A, Device B, and Device C, respectively, corresponding to a 73%

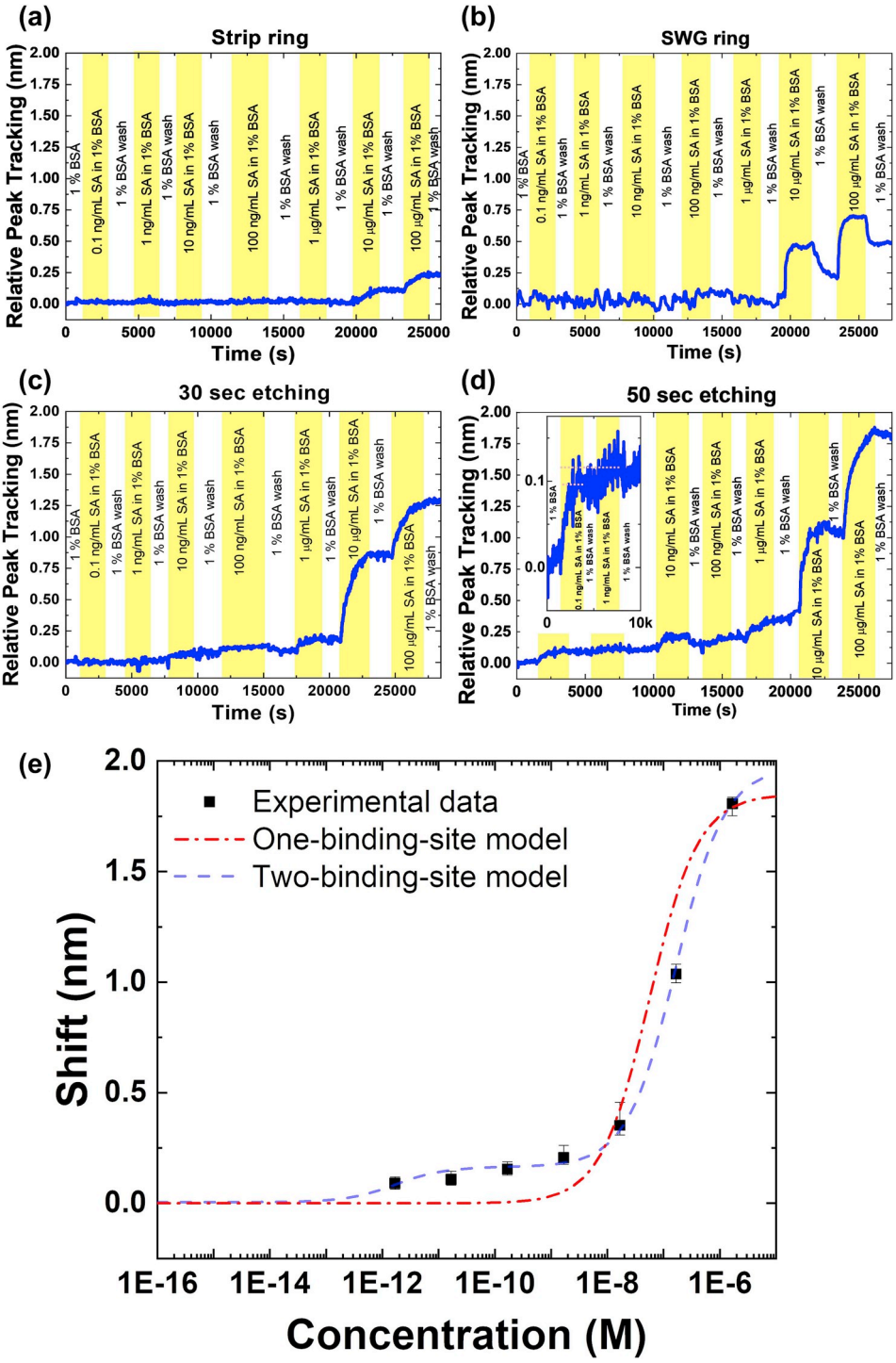

Fig. 6. The real-time relative resonance peak monitored of streptavidin detection for (a) strip microring resonator, (b) regular SGM microring resonators, (c) 30 s and (d) 50 s etched pedestal SGM microring resonators. (e) A wavelength shifts as a function of streptavidin concentration for one-site binding model and two-site binding model fittings.

improvement after forming the pedestal structures. After PBS wash process, the resonance shifts of strip microring resonator, Device A, Device B, and Device C are 0.06 nm, 0.17 nm, 0.37 nm, and 0.49 nm, respectively. It was noticed that Device C has more than doubled peak shift compared to regular SGM microring resonator (Device A) fabricated in this study and over six-time peak shift enhancement than strip microring resonator (Hoste et al., 2014).

4.3. The real-time measurement of streptavidin (SA) detection

Similar as NHS-biotin immobilization, PBS with 1% BSA, 0.1 ng/mL, 1 ng/mL, 10 ng/mL, 100 ng/mL, 1 µg/mL, 10 µg/mL, and 100 µg/mL of streptavidin diluted with PBS + 1% BSA were introduced sequentially through PDMS microfluidic channel with a flow rate of 20 µL/min. Furthermore, PBS with 1% BSA was also injected into the sensing area between two different concentrations to eliminate unbinding streptavidin for resonance peak shift analysis. Fig. 6 (a)-(d) are

real-time monitor of the relative resonance peak shifts for strip microring resonator, regular SGM microring resonators, 30 s and 50 s etched pedestal SGM microring resonators, respectively. The k_a and k_d are calculated as $\sim 5 \times 10^7\ M^{-1}s^{-1}$ and $\sim 6 \times 10^{-8}\ s^{-1}$ (Heidari et al., 2014). It is remarkable that a low concentration of 0.1 ng/mL (~1.67 pM) was detected by Device C with 50 s etched pedestal. Moreover, the experimental streptavidin limit of detection for strip microring resonator, regular SGM microring resonators, and Device B are 10 μg/mL, 100 ng/mL, and 10 ng/mL respectively. That signifies not only the bulk sensitivity enhancement but also streptavidin limit of detection of biosensing improvement due to the increased interaction between the optical field and analytes in SGM microring resonators with the pedestal structure.

The two-site binding model (Chakravarty et al., 2014b) are considered in this study due to mismatched fitting based on the one-site binding model. The chemical equations of two-site binding model are described as below and the theoretical fitting of response shift versus concentration varied streptavidin is expressed in Fig. 6 (e).

$$[\text{biotin}]_{\text{site 1}} + [\text{streptavidin}] \leftrightarrow [\text{biotin} \cdot \text{streptavidin}]_{\text{site 1}}\ K_{D1} \quad (4)$$

$$[\text{biotin}]_{\text{site 2}} + [\text{streptavidin}] \leftrightarrow [\text{biotin} \cdot \text{streptavidin}]_{\text{site 2}}\ K_{D2} \quad (5)$$

$$\Delta\lambda = \frac{\Delta\lambda_{\max 1}}{\left(\frac{K_{D1}}{[\text{streptavidin}]} + 1\right)} + \frac{\Delta\lambda_{\max 2}}{\left(\frac{K_{D2}}{[\text{streptavidin}]} + 1\right)} \quad (6)$$

To compare two models, the fitting curves are the red dash dot line (one-site binding model) and the blue dash line (two-site binding model), respectively. The two-site binding model fits well with a regression correlation coefficient $r^2 = 0.997$. The dissociation constants K_{D1} and K_{D2} for two-site binding on a receptor are 1.76×10^{-12} M and 1.73×10^{-7} M, respectively. According to the fitting results, the streptavidin limit of detection which considered biomolecule interaction may be expected to be ~400 fM with ± 0.03 nm error based on the 1.67 pM results using a 0.01 nm resolution spectra analyzer.

5. Conclusions

The sensitivity of a sensor depends upon the interaction between the optical field and analytes. Many methods have been proposed to maximize the interaction which is ultimately limited by the asymmetric index profile of the silicon-on-insulator platform. In this paper, pedestaled subwavelength grating metamaterial microring resonators are proposed to reduce the asymmetricity and improve the sensitivity. The theoretical analysis and simulation show that the sensitivity can be improved significantly. Enhanced bulk sensitivity and limit of detection are demonstrated experimentally. Real-time monitoring of the resonance shift measurement shows the detection of streptavidin at a low concentration of 0.1 ng/mL (~1.67 pM) by the portable optical spectrum analyzer with 0.15 nm resolution. In addition, the device can potentially detect even lower concentration of streptavidin (~400 *f*M) with higher resolution optical spectrum analyzer. These demonstrations prove that the pedestaled subwavelength grating metamaterial microring resonator is a promising platform for the detection of any refractive index perturbations, such as biomarker detection and chemical detection. Leveraging the microelectronics fabrication capability, the proposed ring resonator could be multiplexed in a large scale, which could make it a very competitive alternative to existing measurement methods, such as enzyme-linked immunosorbent assay (ELISA).

Declaration of interests

The authors declare that they have no known competing financial interests or personal relationships that could have appeared to influence the work reported in this paper.

Conflict of interest

The authors declare that we do not have any commercial or associative interest that represents a conflict of interest in connection with the work submitted.

CRediT authorship contribution statement

Ching-Wen Chang: Data curation, Formal analysis, Writing - original draft. **Xiaochuan Xu:** Supervision, Conceptualization, Formal analysis, Writing - original draft, Funding acquisition. **Swapnajit Chakravarty:** Supervision. **Hui-Chun Huang:** Data curation. **Li-Wei Tu:** Supervision, Writing - review & editing, Funding acquisition. **Quark Yungsung Chen:** Funding acquisition. **Hamed Dalir:** Funding acquisition. **Michael A. Krainak:** Funding acquisition. **Ray T. Chen:** Supervision, Conceptualization, Writing - review & editing, Funding acquisition.

Acknowledgments

This work was supported by NASA STTR program (80NSSC18P2146), the U.S. Department of Energy SBIR program (DE SC-0013178), AFOSR MURI program (FA9550-08-1-0394), National Cancer Institute/National Institutes of Health (NCI/NIH) (Contract #: 1R43HG009113-01A1) and the Ministry of Science and Technology, Taiwan, ROC (106-2911-I-110-503).

The idea is conceived by Xiao-chuan Xu and Ray T. Chen. The device is fabricated and tested by Ching-Wen Chang, under the supervision of Xiao-chuan Xu and Li-Wei Tu. Xiao-chuan Xu writes the theoretical part of the manuscript; Ching-Wen Chang writes the experimental part with input from Li-Wei Tu. TEM fine cross-section images are taken by Hui-Chun Huang. Hamed Dalir and Ray Chen serves as the principle investigators for the NASA STTR biosensor program with Michael A. Krainak as the program monitor who involved in the technical discussion.

Appendix A. Supplementary data

Supplementary data to this article can be found online at https://doi.org/10.1016/j.bios.2019.111396.

References

Azuelos, P., Girault, P., Lorrain, N., Dumeige, Y., Bodiou, L., Poffo, L., Guendouz, M., Thual, M., Charrier, J., 2018. Optimization of porous silicon waveguide design for micro-ring resonator sensing applications. J. Opt. 20 (8) 085301.

Benedikovic, D., Berciano, M., Alonso-Ramos, C., LeRoux, X., Cassan, E., Marris-Morini, D., Vivien, L., 2017. Dispersion control of silicon nanophotonic waveguides using sub-wavelength grating metamaterials in near- and mid-IR wavelengths. Optic Express 25 (16), 19468.

Björquist, P., Boström, S., 1997. Determination of the kinetic constants of tissue factor/factor VII/factor VIIA and antithrombin/heparin using surface plasmon resonance. Thromb. Res. 85 (3), 225–236.

Bock, P.J., Cheben, P., Schmid, J.H., Lapointe, J., Delâge, A., Janz, S., Aers, G.C., Xu, D., Densmore, A., Hall, T.J., 2010. Subwavelength grating periodic structures in silicon-on-insulator: a new type of microphotonic waveguide Przemek. Optic Express 18 (19), 20251.

Chakravarty, S., Hosseini, A., Xu, X., Zhu, L., Zou, Y., Chen, R.T., 2014a. Analysis of ultra-high sensitivity configuration in chip-integrated photonic crystal microcavity biosensors. Appl. Phys. Lett. 104, 191109.

Chakravarty, S., Hosseini, A., Xu, X., Zhu, L., Zou, Y., Chen, R.T., 2014b. Analysis of ultra-high sensitivity configuration in chip-integrated photonic crystal microcavity biosensors. Appl. Phys. Lett. 104 (19), 191109.

Chakravarty, S., Chen, X., Tang, N., Lai, W., Zou, Y., Yan, H., Chen, R.T., 2016. Review of design principles of 2D photonic crystal microcavity biosensors in silicon and their applications. Front. Optoelectron. 9 (2), 206–224.

Chang, C., Chen, P., Wang, S., Hsu, S., Hsu, W., Tsai, C., VWadekar, P., Puttaswamy, S., Cheng, K., Hsieh, S., Wang, H.J., Kuo, K., Sun, Y., Tu, L., 2018. Sensors and Actuators B : chemical Fast detection of tumor marker CA 19-9 using AlGaN/GaN high electron mobility transistors. Sensor. Actuator. B Chem. 267, 191–197.

Chao, C.Y., Fung, W., Guo, L.J., 2006. Polymer microring resonators for biochemical sensing applications. IEEE J. Sel. Top. Quantum Electron. 12 (1), 134–142.

Cheben, P., Xu, D., Janz, S., Densmore, A., 2006. Subwavelength waveguide grating for mode conversion and light coupling in integrated optics. Optic Express 14 (11), 4695.
Cheben, P., Bock, P.J., Schmid, J.H., Lapointe, J., Janz, S., Xu, D.-X., Densmore, A., Delâge, A., Lamontagne, B., Hall, T.J., 2010. Refractive index engineering with subwavelength gratings for efficient microphotonic couplers and planar waveguide multiplexers. Opt. Lett. 35 (15), 2526.
Cheben, P., Halir, R., Schmid, J.H., Atwater, H.A., Smith, D.R., 2018. Subwavelength integrated photonics. Nature 560 (7720), 565–572.
Claes, T., Molera, J.G., DeVos, K., Schacht, E., Baets, R., Bienstman, P., 2009. Label-free biosensing with a slot-waveguide-based ring resonator in silicon on insulator. IEEE Photonics J 1 (3), 197–204.
DeVos, K., Bartolozzi, I., Schacht, E., Bienstman, P., Baets, R., 2007. Silicon-on-Insulator microring resonator for sensitive and label-free biosensing. Optic Express 15 (12), 7610.
Donzella, V., Sherwali, A., Flueckiger, J., Grist, S.M., Fard, S.T., Chrostowski, L., 2015. Design and fabrication of SOI micro-ring resonators based on sub-wavelength grating waveguides. Optic Express 23 (4), 4791.
Dostálek, J., Huang, C.J., Knoll, W., 2009. Surface Design: Applications in Bioscience and Nanotechnology. Wiley-VCH Verlag GmbH & Co. KGaA.
Fägerstam, L.G., Frostell-Karlsson, Å., Karlsson, R., Persson, B., Rönnberg, I., 1992. Biospecific interaction analysis using surface plasmon resonance detection applied to kinetic, binding site and concentration analysis. J. Chromatogr. A 597 (1–2), 397–410.
Fan, Y., Ding, Y., Ma, H., Teramae, N., Sun, S., He, Y., 2015. Optical waveguide sensor based on silica nanotube arrays for label-free biosensing. Biosens. Bioelectron. 67, 230–236.
Fard, S.T., Donzella, V., Schmidt, S.A., Flueckiger, J., Grist, S.M., Talebi Fard, P., Wu, Y., Bojko, R.J., Kwok, E., Jaeger, N.A.F., Ratner, D.M., Chrostowski, L., 2014. Performance of ultra-thin SOI-based resonators for sensing applications. Optic Express 22 (12), 14166.
Flueckiger, J., Schmidt, S., Donzella, V., Sherwali, A., Ratner, D.M., Chrostowski, L., Cheung, K.C., 2016. Sub-wavelength grating for enhanced ring resonator biosensor. Optic Express 24 (14), 15672.
Gaur, G., Hu, S., Mernaugh, R.L., Kravchenko, I.I., Retterer, S.T., Weiss, S.M., 2018. Label-free detection of Herceptin®using suspended silicon microring resonators. Sensor. Actuator. B Chem. 275 (July), 394–401.
Gavela, A.F., García, D.G., Ramirez, J.C., Lechuga, L.M., 2016. Last advances in silicon-based optical biosensors. Sensors 16, 1–15.
Ghasemi, F., Hosseini, E.S., Song, X., Gottfried, D.S., Chamanzar, M., Raeiszadeh, M., Cummings, R.D., Eftekhar, A.A., Adibi, A., 2016. Multiplexed detection of lectins using integrated glycan-coated microring resonators. Biosens. Bioelectron. 80, 682–690.
Gonzalo Wangüemert-Pérez, J., Cheben, P., Ortega-Moñux, A., Alonso-Ramos, C., Pérez-Galacho, D., Halir, R., Molina-Fernández, I., Xu, D.-X., Schmid, J.H., 2014. Evanescent field waveguide sensing with subwavelength grating structures in silicon-on-insulator. Opt. Lett. 39 (15), 4442.
Heidari, A., Yoon, Y.J., Park, W.T., Su, P.C., Miao, J., Ming Lin, J.T., Park, M.K., 2014. Biotin-streptavidin binding interactions of dielectric filled silicon bulk acoustic resonators for smart label-free biochemical sensor applications. Sensors 14 (3), 4585–4598.
Hoste, J.-W., Werquin, S., Claes, T., Bienstman, P., 2014. Conformational analysis of proteins with a dual polarisation silicon microring. Optic Express 22 (3), 2807.
Huang, L., Yan, H., Xu, X., Chakravarty, S., Tang, N., Tian, H., Chen, R.T., 2017. Improving the detection limit for on-chip photonic sensors based on subwavelength grating racetrack resonators. Optic Express 25 (9), 10527.
Iqbal, M., aGleeson, M., Spaugh, B., Tybor, F., Gunn, W.G., Hochberg, M., Baehr-jones, T., Bailey, R.C., Gunn, L.C., 2010. Label-free biosensor arrays based on silicon ring resonators and high-speed optical scanning instrumentation. IEEE J. Sel. Top. Quantum Electron. 16 (3), 654–661.
Jin, Z., Guan, W., Liu, C., Xue, T., Wang, Q., Zheng, W., Cui, X., 2016. A stable and high resolution optical waveguide biosensor based on dense TiO 2/Ag multilayer film. Appl. Surf. Sci. 377, 207–212.
Kim, K.W., Song, J., Kee, J.S., Liu, Q., Lo, G.Q., Park, M.K., 2013. Label-free biosensor based on an electrical tracing-assisted silicon microring resonator with a low-cost broadband source. Biosens. Bioelectron. 46, 15–21.
Köser, J., Wriedt, T., 1999. Refractive-index measurements in the near-IR using an Abbe refractometer Refractive-index measurements in the near-IR using an Abbe refractometer. Meas. Sci. Technol. 8 (March 2017), 601.
Lin, P.T., Singh, V., Hu, J., Richardson, K., Musgraves, J.D., Luzinov, I., Hensley, J., Kimerling, L.C., Agarwal, A., 2013a. Chip-scale Mid-Infrared chemical sensors using air-clad pedestal silicon waveguides. Lab Chip 13 (11), 2161.
Lin, P.T., Singh, V., Cai, Y., Kimerling, L.C., Agarwal, A., 2013b. Air-clad silicon pedestal structures for broadband mid-infrared microphotonics. Opt. Lett. 38 (7), 1031–1033.
Luan, E., Shoman, H., Ratner, D.M., Cheung, K.C., Chrostowski, L., 2018. Silicon photonic biosensors using label-free detection. Sensors 18 (10), 1–42.
Luchansky, M.S., Bailey, R.C., 2012. High-Q optical sensors for chemical and biological analysis. Anal. Chem. 84 (2), 793–821.
Lueckiger, J.O.F., Chmidt, S.H.O.N.S., Onzella, V.A.D., Herwali, A.H.S., Atner, D.A.M.R., Hrostowski, L.U.C., Heung, K.A.C.C., 2016. Sub-wavelength grating for enhanced ring resonator biosensor. Optic Express 24 (14), 19912–19920.
McClellan, M.S., Domier, L.L., Bailey, R.C., 2012. Label-free virus detection using silicon photonic microring resonators. Biosens. Bioelectron. 31 (1), 388–392.
Miyazaki, C.M., Shimizu, F.M., Mejía-Salazar, J.R., Oliveira, O.N., Ferreira, M., 2017. Surface plasmon resonance biosensor for enzymatic detection of small analytes. Nanotechnology 28 (14), 145501.
Myszka, D.G., He, X., Dembo, M., Morton, T.A., Goldstein, B., 1998. Extending the range of rate constants available from BIACORE: interpreting mass transport-influenced binding data. Biophys. J. 75, 583–594.
Oser, D., Pérez-Galacho, D., Alonso-Ramos, C., LeRoux, X., Tanzilli, S., Vivien, L., Labonté, L., Cassan, É., 2018. Subwavelength engineering and asymmetry: two efficient tools for sub-nanometer-bandwidth silicon Bragg filters. Opt. Lett. 43 (14), 3208.
Penades, J.S., Ortega-Moñux, A., Nedeljkovic, M., Wangüemert-Pérez, J.G., Halir, R., Khokhar, A.Z., Alonso-Ramos, C., Qu, Z., Molina-Fernández, I., Cheben, P., Mashanovich, G.Z., 2016. Suspended silicon mid-infrared waveguide devices with subwavelength grating metamaterial cladding. Optic Express 24 (20), 22908.
Penadés, J.S., Sánchez-Postigo, A., Nedeljkovic, M., Ortega-Moñux, A., Wangüemert-Pérez, J.G., Xu, Y., Halir, R., Qu, Z., Khokhar, A.Z., Osman, A., Cao, W., Littlejohns, C.G., Cheben, P., Molina-Fernández, I., Mashanovich, G.Z., 2017. Suspended silicon waveguides for long-wave infrared wavelengths. Opt. Lett. 43 (4), 795.
Rodriguez, G.A., Hu, S., Weiss, S.M., 2015. Porous silicon ring resonator for compact, high sensitivity biosensing applications. Optic Express 23 (6), 7111.
Soler Penadés, J., Alonso-Ramos, C., Khokhar, A.Z., Nedeljkovic, M., Boodhoo, L.A., Ortega-Moñux, A., Molina-Fernández, I., Cheben, P., Mashanovich, G.Z., 2014. Suspended SOI waveguide with sub-wavelength grating cladding for mid-infrared. Opt. Lett. 39 (19), 5661.
Tu, X., Song, J., Liow, T.-Y., Park, M.K., Yiying, J.Q., Kee, J.S., Yu, M., Lo, G.-Q., 2012. Thermal independent Silicon-Nitride slot waveguide biosensor with high sensitivity. Optic Express 20 (3), 2640.
Wangüemert-Pérez, J.G., Hadij-ElHouati, A., Sánchez-Postigo, A., Leuermann, J., Xu, D.X., Cheben, P., Ortega-Moñux, A., Halir, R., Molina-Fernández, Í., 2019. Subwavelength structures for silicon photonics biosensing. Optic Laser. Technol. 109, 437–448.
Washburn, A.L., Gunn, L.C., Bailey, R.C., 2009. Label-free quantitation of a cancer biomarker in complex media using silicon photonic microring resonators. Anal. Chem. 81 (22), 9499–9506.
Xu, X., 2013. Silicon Nanomembrane for High Performance Conformal Photonic Devices. The University of Texas at Austin.
X.Xu and R. T.Chen, "Subwavelength Photonic Crystal Waveguide in Optical Systems," U. S. patent US 2017/0146738A1 (2017)..
Xu, X., Chen, R.T., 2017b. Subwavelength photonic crystal waveguide with trapezoidal shaped dielectric pillars in optical systems. U.S. patent US 9 563,016 B1.
Xu, D., Densmore, A., Delâge, A., Waldron, P., Mckinnon, R., Janz, S., Lapointe, J., Lopinski, G., Mischki, T., Post, E., Cheben, P., Schmid, J.H., 2008. Folded cavity SOI microring sensors for high sensitivity and real time measurement of biomolecular binding. Optic Express 16 (19), 15137–15148.
Yalçin, A., Popat, K.C., Aldridge, J.C., Desai, T.A., Hryniewicz, J., Chbouki, N., Little, B.E., King, O., Van, V., Chu, S., Gill, D., Anthes-Washburn, M., Ünlü, M.S., Goldberg, B.B., 2006. Optical sensing of biomolecules using microring resonators. IEEE J. Sel. Top. Quantum Electron. 12 (1), 148–154.
Yan, H., Zou, Y., Chakravarty, S., Yang, C., Wang, Z., Tang, N., Fan, D., Chen, R.T., 2015. Silicon on-chip bandpass filters for the multiplexing of high sensitivity photonic crystal microcavity biosensors Silicon on-chip bandpass filters for the multiplexing of high sensitivity photonic crystal microcavity biosensors. Appl. Phys. Lett. 106, 121103.
Yan, H., Huang, L., Xu, X., Chakravarty, S., Tang, N., Tian, H., Chen, R.T., 2016. Unique surface sensing property and enhanced sensitivity in microring resonator biosensors based on subwavelength grating waveguides. Optic Express 24 (26), 29724.
Zhang, Z., Ng, G.I., Hu, T., Qiu, H., Guo, X., Wang, W., Rouifed, M.S., Liu, C., Sia, J., Zhou, J., Littlejohns, C.G., Reed, G.T., Wang, H., 2018. Mid-Infrared sensor based on a suspended microracetrack resonator with lateral subwavelength-grating metamaterial cladding. IEEE Photonics J 10 (2), 1–8.
Zhao, C.Y., Zhang, L., Zhang, C.M., 2018. Compact SOI optimized slot microring coupled phase-shifted Bragg grating resonator for sensing. Optic Commun. 414 (September 2017), 212–216.
Zou, Y., Chakravarty, S., Member, S., Kwong, D.N., Lai, W., Xu, X., Lin, X., Hosseini, A., Chen, R.T., 2014. Cavity-waveguide coupling engineered high sensitivity silicon photonic crystal microcavity biosensors with high yield. IEEE J. Sel. Top. Quantum Electron. 20 (4).